Tau^{IQ}: A Canonical Image Based Algorithm to Quantify Tau PET Scans

Alex Whittington[1] and Roger N. Gunn[1,2] for the Alzheimer's Disease Neuroimaging Initiative

[1]*Invicro LLC, London, United Kingdom; and* [2]*Department of Brain Sciences, Imperial College London, Hammersmith Hospital Campus, London, United Kingdom*

Recently, Amyloid^{IQ} was introduced as a new canonical image-based algorithm to quantify amyloid PET scans and demonstrated increased power over traditional SUV ratio (SUVR) approaches when assessed in cross-sectional and longitudinal analyses. We build further on this mathematical framework to develop a Tau^{IQ} algorithm for the quantitative analysis of the more complex spatial distribution displayed by tau PET radiotracers. **Methods:** Cross-sectional (n = 615) and longitudinal (n = 149) ^{18}F-flortaucipir data were obtained from the Alzheimer's Disease Neuroimaging Initiative along with necessary adjunct amyloid PET and T1-weighted structural MRI data. A subset of these data were used to derive a chronological tau dataset, using Amyloid^{IQ} analysis of associated amyloid PET data to calculate the subject's temporal position in the canonical AD disease process, from which canonical images for the nonspecific and specific binding components of ^{18}F-flortaucipir in AD were calculated. These 2 canonical images were incorporated into the Tau^{IQ} algorithm that enables the quantification of both global and local tau outcome measures using an image-based regression and statistical parametric analysis of the initial residual image. Performance of the Tau^{IQ} algorithm was compared with SUVR approaches for cross-sectional analyses, longitudinal analyses, and correlation with clinical measures (Alzheimer Disease Assessment Scale–Cognitive Subscale [ADAS-Cog], Clinical Dementia Rating scale–sum of boxes [CDR-SB], and Mini-Mental State Examination [MMSE]). **Results:** Tau^{IQ} successfully calculated global tau load (Tau$_L$) in all 791 scans analyzed (range, −3.5% to 185.2%; mean ± SD, 23% ± 20.5%) with a nonzero additional local tau component being required in 31% of all scans (cognitively normal [CN], 22%; mild cognitive impairment [MCI], 35%; dementia, 72%). Tau^{IQ} was compared with the best SUVR approach in the cross-sectional analysis (Tau$_L$ increase in effect size: CN− vs. CN+, +45%; CN− vs. MCI+, −5.6%; CN− vs. dementia+, +2.3%) (+/− indicates amyloid-positive or -negative) and correlation with clinical scores (Tau$_L$ increase in r^2: CDR-SB+, 7%; MMSE+, 38%; ADAS-Cog+, 0%). Tau^{IQ} substantially outperformed SUVR approaches in the longitudinal analysis (Tau^{IQ} increase in power: CN+, >3.2-fold; MCI+, >2.2-fold; dementia+, >2.9-fold). **Conclusion:** Tau$_L$ as calculated by Tau^{IQ} provides a superior approach for the quantification of tau PET data. In particular, it provides a substantial improvement in power for longitudinal analyses and the early detection of tau deposition and thus should have significant value for clinical imaging trials in AD that are investigating the attenuation of tau deposition with novel therapies.

Key Words: statistical analysis; canonical images; flortaucipir; IQ platform; power in clinical trials; tau PET

Received Oct. 20, 2020; revision accepted Jan. 13, 2021.

For correspondence or reprints, contact Alex Whittington (alexander.whittington@invicro.co.uk).

Published online January 30, 2021.

J Nucl Med 2021; 62:1292–1300
DOI: 10.2967/jnumed.120.258962

Tau and amyloid-β (Aβ) are the 2 pathologic hallmarks of Alzheimer disease and consequently represent 2 key targets for both drug and biomarker development. The development of Aβ PET biomarkers and their associated analytics is well advanced, with established Food and Drug Administration–approved ^{18}F radiotracers (^{18}F-florbetapir, ^{18}F-florbetaben, and ^{18}F-flutemetamol) available after the pioneering work with ^{11}C-Pittsburgh compound B that originated in 2004 (*1*). In parallel, analytic approaches for Aβ agents have advanced from historical SUV ratio (SUVR) methods to the development of centiloids, which allow for conversion of different amyloid agents onto a common scale facilitating their combined use in multicenter imaging trials (*2*). Further, our previous work using spatiotemporal modeling of Aβ accumulation in AD (*3*) deduced that amyloid accumulation is a global process that can be characterized by a single parameter (Aβ$_L$) and opened the door for the canonical image based quantification used by Amyloid^{IQ}, which has shown increased power over SUVR-based methods in both cross-sectional and longitudinal analyses (*4*).

The development of tau imaging agents faced increased challenges due to lower target density, selectivity issues over off-target species, and the existence of different isomeric forms of tau (3*R*,4*R*) and gained traction in the following decade only with the introduction of ^{18}F-flortaucipir in 2013 (*5*). After this breakthrough, other tau imaging agents have been developed that demonstrate the ability to measure tau deposition in human subjects, including ^{18}F-MK-6240 (*6*), ^{18}F-GTP-1 (*7*), ^{18}F-RO-948 (*8*), ^{18}F-PI-2620 (*9*), and ^{18}F-APN-1607 (*10*), and in May 2020 ^{18}F-flortaucipir was Food and Drug Administration–approved as a radioactive diagnostic agent for adults with cognitive impairment who are being evaluated for Alzheimer disease (*11,12*).

To date, analytic approaches for static tau PET imaging have focused on SUVR approaches, with tau-relevant regions of interest (ROIs) being used to quantify the level of tau deposition in regions corresponding to the different stages of tau accumulation described in the postmortem work of Braak and Braak (*13*). This includes the use of regions that correspond to Braak stages I–VI and meta-ROIs that consider the initial or strongest areas of deposition (the transentorhinal cortex and other temporal regions (*13*)), such as the temporal meta-ROI of Jack et al. (*14*). These SUVR methods have been applied to cross-sectional (*15–18*) and longitudinal (*14,19–21*) data to show an increase in tau signals associated with disease progression in AD.

The present work extends the prior analytic concepts of Amyloid^{IQ} further to account for the more complex spatiotemporal distribution of tau to develop an algorithm for the quantification of tau PET scans (Tau^{IQ}). Initial investigations of tau PET scans found that the accumulation in many subjects was more complex, with evidence of additional hot spots of local tau deposition. This finding led to the development of an algorithm that can accurately quantify both the global tau accumulation pattern (as with amyloid) and any additional subject-specific localized deposits sitting on top of this pattern. The current work first describes the development of the Tau^{IQ} algorithm and then compares its performance with SUVR approaches for cross-sectional analyses, longitudinal analyses, and correlation with clinical measures using ^{18}F-flortaucipir data obtained from the Alzheimer's Disease Neuroimaging Initiative (ADNI).

MATERIALS AND METHODS

Imaging Data

Imaging data were obtained from the ADNI database (*22*). ADNI was launched in 2003 as a public–private partnership, led by Principal Investigator Michael W. Weiner. The primary goal of ADNI has been to test whether serial MRI, PET, other biologic markers, and clinical and neuropsychologic assessment can be combined to measure the progression of mild cognitive impairment (MCI) and early AD. Up-to-date information is available at www.adni-info.org.

Data for Development of Tau^{IQ} Canonical Images

Baseline ^{18}F-flortaucipir PET, ^{18}F-florbetapir PET, and structural T1-weighted MRI scans were obtained for 233 subjects (127 cognitively normal [CN], 82 with MCI, and 24 with dementia; 118 men and 114 women; mean age ± SD, 76.4 y [range, 61.3–94.4 y]; Clinical Dementia Rating scale–sum-of-boxes [CDR-SB] score, 0.88 ± 1.12 [range, 0–5.5]; Mini-Mental State Examination [MMSE] score, 26.7 ± 1.7 [range, 20–30]; Alzheimer Disease Assessment Scale–Cognitive Subscale (ADAS-Cog) score, 16.4 ± 8.7 [range, 2–52.0]).

Cross-Sectional Testing Data

To create a more comprehensive dataset for testing, 382 additional ADNI subjects were added to the development dataset, for a total of 615 subjects (382 CN, 175 with MCI, and 58 with dementia; 290 men and 325 women; age, 74.1± 7.7 y [range, 56.0–94.4 y], CDR-SB score, 0.77 ± 1.28 [range, 0–8]; MMSE score, 28.5 ± 2.0 [range, 17–30]; ADAS-Cog score, 16.0 ± 8.1 [range, 2–52]). For these additional subjects, a ^{18}F-flortaucipir scan, a static amyloid PET scan (^{18}F-florbetapir or ^{18}F-florbetaben), and a structural T1-weighted MRI scan were obtained.

Longitudinal Testing Data

From the cross-sectional dataset, 149 subjects (88 CN, 43 with MCI, and 18 with dementia; 76 men and 72 women; age, 74.5 ± 7.4 y [range, 56.3–92.2 y]; CDR-SB score, 0.89 ± 1.42 [range, 0–8]; MMSE score, 28.2 ± 2.3 [range, 17–30]; ADAS-Cog score, 16.5 ± 8.5 [range, 5.3–44.7] at baseline) also had sequential ^{18}F-flortaucipir PET scans (1 or 2 follow-up visits: 121 subjects had 1 follow-up visit and 27 had 2 follow-up visits) between 4 mo and 2.5 y after baseline, which were used for the longitudinal analysis.

Image Acquisition and Preprocessing

All human PET data were acquired in accordance with the standardized ADNI protocol (*23*). ^{18}F-flortaucipir PET scans consisted of emission data from a 30-min (six 5-min frames) acquisition at 75 min after injection, with an injected dose of 370 MBq ± 10%. ^{18}F-florbetapir data consisted of emission data from a 20-min (four 5-min frames) acquisition collected 50 min after injection, with an injected dose of 370 MBq ± 10%. ^{18}F-florbetaben data consisted of emission data from a 20-min (four 5-min frames) acquisition collected 90 min after injection, with an injected dose of 300 MBq ± 10%. Three image-preprocessing steps were applied to the data before entry into the ADNI imaging database (full details are described at http://adni.loni.usc.edu/methods/pet-analysis/preprocessing). Briefly, the frames were coregistered and averaged. The resulting image was converted to a 160 × 160 × 96 voxel static image with voxel dimensions of 1.5 × 1.5 × 1.5 mm. Finally, a gaussian filter (of ≤6 mm) was applied to harmonize the image resolution with the lowest-resolution scanner used in the study. All subjects also underwent T1-weighted structural MRI. These primary PET and MRI data were downloaded from the ADNI database and used in the subsequent analyses.

Image Processing

Registration of Images into Stereotactic Space. ^{18}F-flortaucipir, ^{18}F-florbetapir, and ^{18}F-florbetaben data were nonlinearly registered into Montreal Neurological Institute template 152 (MNI152) space (*24*) using the subjects' T1-weighted MRI scan as part of a diffeomorphic nonlinear registration (Diffeomorphic Anatomical Registration using Exponentiated Lie algebra [DARTEL]) (*25*). Initially, the structural MR images were segmented into gray matter and white matter using SPM, version 12. DARTEL then uses these tissue probability maps to create flow fields that provide the parameters required to spatially normalize any images that are coregistered to the MR image into MNI152 space. Each PET image is registered to the corresponding MRI scan using a rigid-body registration, and the individuals' DARTEL flow-field is applied without modulation, resulting in ^{18}F-flortaucipir, ^{18}F-florbetapir, and ^{18}F-florbetaben images in MNI152 space. The normalized maps are spatially smoothed (gaussian kernel of 8 mm in full width at half maximum).

Generation of SUVR Images. SUVR images for ^{18}F-flortaucipir were generated using the ventrolateral cerebellum of the CIC atlas (*26*) as the reference region by dividing all intensities in the image by the mean uptake value for the ventrolateral cerebellum ROI.

Development of Tau^{IQ} Algorithm

Creation of Chronological ^{18}F-Flortaucipir Dataset and Derivation of Canonical Images. For each subject in the development dataset, Amyloid^{IQ} was performed on the subject's ^{18}F-florbetapir scan to obtain the subject's amyloid load ($A\beta_L$). Using a previously published functional form, F, describing the temporal accumulation of $A\beta_L$ in AD (*27*), it was possible to derive the time, T, through the amyloid accumulation process as $T = F^{-1}(A\beta_L)$, which lies in the interval of 0–30 y. This process was repeated for all subjects to produce an estimated time for each of them in the amyloid accumulation process. These times were subsequently associated with each subject's corresponding ^{18}F-flortaucipir tau PET scan (Fig. 1A).

Next, a linear regression was fitted at the voxel level to the chronological ^{18}F-flortaucipir PET dataset to estimate the canonical images **K** and **NS**. The intercept of the linear regression is the nonspecific (**NS**) value for that voxel, and the carrying capacity (**K**) is 30 multiplied by the gradient so that a scan with 100% global tau load (Tau_L) will correspond to a subject with the expected level of tau observed at the 30-y time point in the amyloid accumulation process (Fig. 1B). In a final step, the carrying-capacity image was made symmetric by averaging the intensities in the left and right hemispheres.

Tau^{IQ} Algorithm. The Tau^{IQ} algorithm decomposes a tau PET scan into nonspecific Tau_L, local tau load ($LTau_L$), and noise using **NS** and **K** and a statistical parametric analysis of an initial residual image (Fig. 2). This process is performed in 2 steps. First, an image-based regression of the tau PET scan with the 2 canonical images is performed in MNI152 space, using QR decomposition in MATLAB,

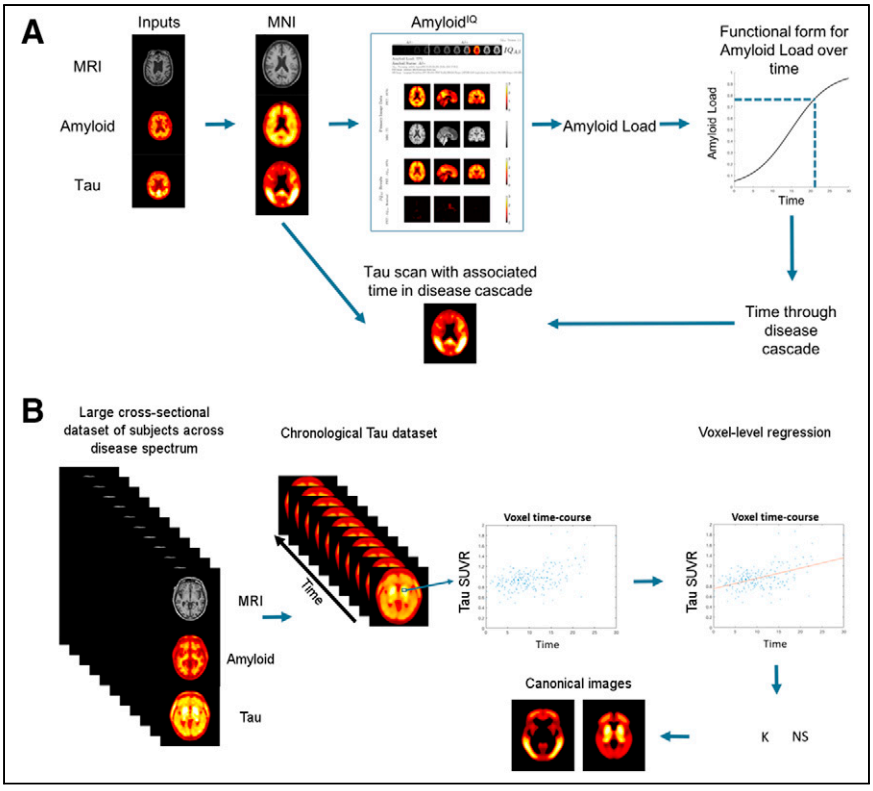

FIGURE 1. Methodology for creating ^{18}F-flortaucipir canonical images. (A) Creation of chronological ^{18}F-flortaucipir dataset using associated ^{18}F-florbetapir data. (B) Generation of ^{18}F-flortaucipir **K** and **NS** canonical images from voxelwise modeling of chronological dataset.

to estimate the Tau_L, the nonspecific scaling factor (ns), and a residual image:

$$SUVr = ns\ NS + Tau_L K. \quad (1)$$

This step is equivalent to Amyloid^{IQ} (*4*) and uses DARTEL (*25*) in the same way to align images into MNI152 space.

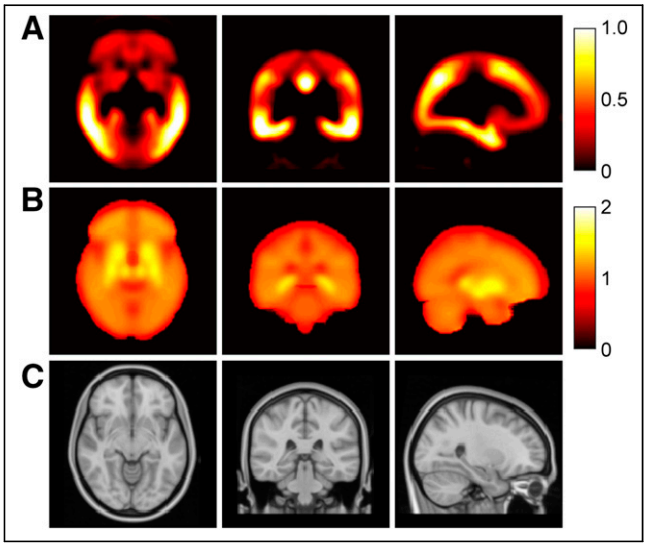

FIGURE 2. Canonical images for ^{18}F-flortaucipir PET derived from spatiotemporal modeling of chronological AD data in MNI152 space: tau canonical image (**K**) (A), nonspecific canonical image (**NS**) (B), and reference structural T1-weighted MR image (C).

Second, the derived residual image is processed via a statistical parametric analysis to estimate an image representing the local tau signal (i.e., signal that is over and above the level of noise expected in the residual image). This statistical parametric analysis uses data derived from a set of amyloid-negative healthy control ^{18}F-flortaucipir scans ($n = 65$), where it is assumed that there is negligible tau, to derive mean and SD images from this set of residual images in order to characterize the noise distribution. These mean and SD images allow for the conversion of a residual image calculated by the first step of Tau^{IQ} to a z score image. This z score image is then processed with the SPM gaussian random fields algorithm (*28*) to estimate clusters of voxels that are significantly greater than zero using a conservative threshold of $P < 0.01$. The $LTau_L$ parameter is then calculated as the 3-dimensional integral of the signal in the local tau image and so is a function of both the intensity and the extent of the local tau signal and has the units $SUVRcm^3$.

Thus, the overall Tau^{IQ} algorithm (Fig. 3) takes as its input a 3-dimensional tau PET image and corresponding structural MRI scan to produce 3 main outputs: the Tau_L, which is the scaling factor for the carrying capacity image (**K**); the local tau image, which shows the local tau signal across the brain; and the $LTau_L$, which is a summary measure of this local signal accounting for both extent and intensity.

Comparison of Tau^{IQ} and SUVR Quantification

The Tau^{IQ} outcome measure Tau_L was compared with SUVR in a cross-sectional analysis, in a longitudinal analysis, and in terms of its relationship with clinical scores (CDR-SB, MMSE, and ADAS-Cog). For all ^{18}F-flortaucipir scans, spatially normalized SUVR images were used to calculate mean regional SUVRs for 4 regions through the application of Jack meta, Braak I/II, Braak III/IV, and Braak V/VI ROIs defined in MNI152 space (Supplemental Fig. 1; supplemental materials are available at http://jnm.snmjournals.org). Amyloid^{IQ} was used to classify each subject as Aβ+ or Aβ− (positive is defined as an $A\beta_L$ greater than 33% (*29*)) to enable subsequent cross-sectional and longitudinal analyses that were stratified for amyloid positivity.

Cross-Sectional Analyses. The Hedges g effect sizes were calculated and compared for group comparisons of CN+ versus CN−, MCI+ versus CN−, and dementia+ versus CN− (+/− indicates amyloid-positive or -negative) using Tau_L and SUVR outcome measures. A 95% CI on the calculated Hedges g was estimated using 10,000 bootstrap replicates of the sample, which was also used to calculate the probability that the outcome measure with the highest effect size in each comparison was superior to all others.

Longitudinal Analyses. A linear regression was performed on the change from baseline of the different outcome measures for each subject, with the intercept constrained to zero. The gradient of this linear regression provides the change per year, and this was recorded for every subject and all analysis approaches. The distributions of the changes per year for the different clinical groups were plotted, and the mean, SD, and effect size (mean divided by SD) were calculated. A 95% CI on the calculated effect size was estimated using 10,000 bootstrap replicates of

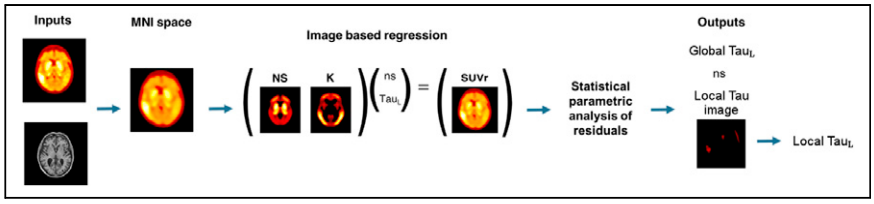

FIGURE 3. Tau^{IQ} algorithm that estimates global and local tau outcome measures.

the sample, which was also used to calculate the probability that the outcome measure with the highest effect size in each clinical group was superior to all others. Finally, the calculated effect size was also used to estimate the sample size required for a clinical trial with an active and placebo arm designed to detect a 25% reduction in tau accumulation in the active arm over 1 y (power = 80%, $\alpha = 0.05$).

Relationship to Clinical Scores. To assess the relationship of the outcome measures Tau$_L$ and SUVR to clinical scores of disease severity, all derived at baseline, correlation analysis (Pearson correlation) was performed with 3 clinical measures: CDR-SB ($n = 615$), MMSE ($n = 615$), and ADAS-Cog ($n = 607$).

RESULTS

Canonical Images

The process of fitting a linear regression at the voxel level to the chronological dataset was performed successfully and produced 2 ^{18}F-flortaucipir canonical images: the tau carrying-capacity image **K** and the nonspecific-binding image **NS** (Fig. 3). The carrying-capacity image exhibited the highest intensities in the temporal and parietal lobe, and the nonspecific-binding image showed the highest intensities in the striatum, which is consistent with some known off-target binding for ^{18}F-flortaucipir in this region (*30,31*).

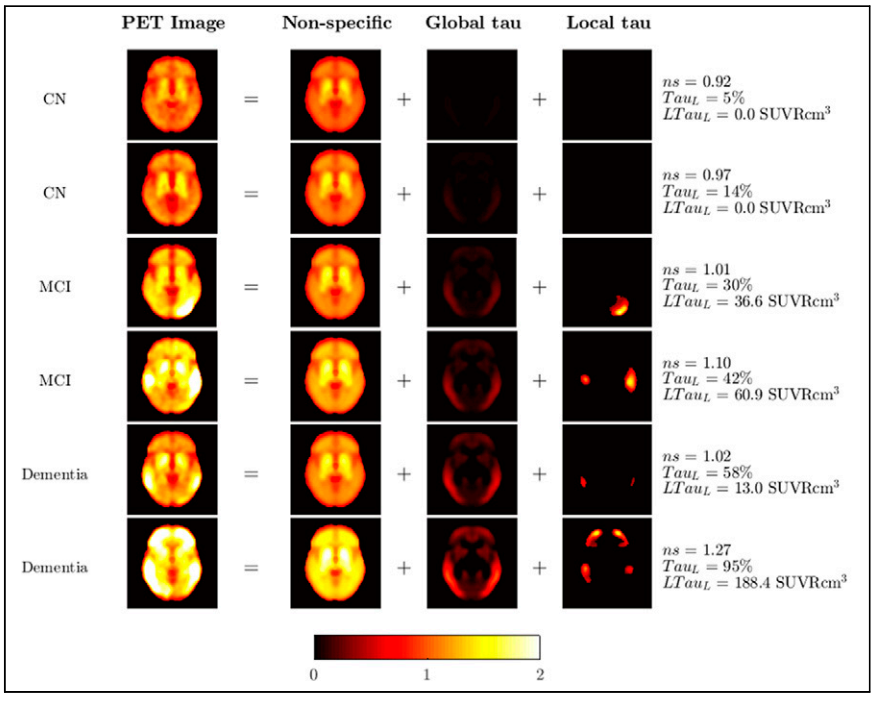

FIGURE 4. Examples of Tau^{IQ} decomposition of ^{18}F-flortaucipir data into nonspecific, global, and local tau signals.

Tau^{IQ}

The Tau^{IQ} algorithm was successfully applied to 791 tau PET scans (488 CN, 226 MCI, and 77 dementia) from cross-sectional and longitudinal datasets and was able to decompose the scans into 3 key components: nonspecific binding, global tau, and local tau. The ^{18}F-flortaucipir signal was well characterized, with the final residual images reflecting noise as expected (representative examples are shown in Fig. 4). Tau$_L$ values estimated across all scans ranged between −3.5% and 185.2% (mean, 21.9% ± 20.4%), and a local tau component was required in 31% of all scans (CN, 22%; MCI, 35%; dementia, 72%).

Cross-Sectional Analysis

Tau$_L$ had the highest effect size for comparison of the CN− and CN+ groups ($P < 0.10$) and an effect size similar to the best SUVR approach for comparison of the CN− and MCI+ groups ($P < 0.64$) and the CN− and dementia+ groups ($P < 0.44$) (Tau$_L$ increase in effect size: CN− vs. CN+, +45%; CN− vs. MCI+, −5.6%; CN− vs. dementia+, +2.3%; Table 1; Fig. 5). Effect sizes among all groups can be found in Supplemental Table 1.

Longitudinal Analysis

The effect size for Tau^{IQ} was greater than that for SUVR in all 6 clinical groups investigated, with the largest value observed in the MCI+ group (Table 2). For Tau^{IQ}, the greatest mean increases per year were also seen in the MCI+ group (3.61%/y), followed by the dementia+ group (2.52%/y) and the CN+ group (2.01%/y). This translated to the MCI+ group's having the lowest clinical trial sample size ($n = 213$ per arm) required to show a 25% attenuation in the accumulation of tau deposition over a 1-y period (power = 80%, $\alpha = 0.05$). Fewer subjects showed a reduction in tau signal over time with Tau^{IQ} than with any of the SUVR measures (34 for Tau$_L$, 61 for SUVR Jack meta-ROI, 68 for SUVR Braak I/II, 57 for SUVR Braak III/IV, 62 for SUVR Braak V/VI; Fig. 6).

Correlation with Clinical Outcome Measures

Analysis of the relationship between the clinical outcome measures (CDR-SB, MMSE, and ADAS-Cog) with both Tau^{IQ} and SUVR outcome measures demonstrated that Tau$_L$ had the strongest relationship with CDR-SB and MMSE (Fig. 7). For ADAS-Cog, the Jack meta-ROI and Tau$_L$ equaled each other in exhibiting the highest correlation ($r^2 = 0.34$).

DISCUSSION

This work extends to tau PET imaging the canonical image-based quantification recently developed for Aβ (Amyloid^{IQ}) (*7*), which has shown increased performance over existing SUVR-based

TABLE 1
Cross-Sectional Analysis*

Outcome measure	CN− vs. CN+	CN− vs. MCI+	CN− vs. dementia+
Tau^{IQ} Tau_L	**1.00 (0.69–1.35), $P < 0.10$**	1.53 (1.21–1.88)	**2.70 (2.28–3.26), $P < 0.44$**
SUVR Jack meta-ROI	0.69 (0.39–1.03)	1.58 (1.21–2.01)	2.64 (2.16–3.27)
SUVR Braak I/II	0.55 (0.26–0.85)	**1.62 (1.24–2.04), $P < 0.64$**	2.46 (1.98–3.03)
SUVR Braak III/IV	0.57 (0.28–0.88)	1.34 (0.99–1.72)	2.37 (1.93–2.92)
SUVR Braak V/VI	0.49 (0.19–0.80)	0.97 (0.63–1.32)	1.90 (1.48–2.40)

*Effect sizes with CIs for ^{18}F-flortaucipir Tau_L and SUVR outcome measures derived from group comparisons. Best-performing method in terms of effect size is highlighted in bold along with probability it is best method.

approaches. The more complex deposition of tau, as compared with Aβ, in AD subjects necessitates the incorporation of a local tau component in the algorithm (with 31% of subjects analyzed in this study requiring the addition of this local tau component).

^{18}F-flortaucipir canonical images characterizing the nonspecific background signal and the global spatial distribution for tau in AD were successfully calculated from a chronological dataset. The nonspecific image, **NS,** is consistent with ^{18}F-flortaucipir images observed in Aβ− healthy controls, from whom tau is absent, demonstrating a homogeneous signal throughout the brain apart from increased uptake in the striatum consistent with known off-target binding of the tracer, which has been linked to monoamine oxidases (*32*). The carrying-capacity image, **K,** is consistent with postmortem maps of tau from AD subjects that show increased deposition in line with Braak staging (*13,33*), with the areas of the temporal lobe that have the highest signal being consistent with the earliest deposition of tau in that region. The Tau^{IQ} algorithm presented here uses these canonical images to determine an estimate of Tau_L (the scaling factor associated with the canonical tau image) and an estimate of $LTau_L$ (any additional tau signal that sits on top of the global tau component).

The performance of the primary Tau^{IQ} outcome parameter (Tau_L) was assessed against current SUVR approaches using common composite ROIs in cross-sectional analysis, longitudinal analysis, and correlation with clinical scores. For the cross-sectional analyses and correlation with clinical outcome measures, Tau^{IQ} typically yielded numerically higher performance metrics than did the best SUVR approach (frequently the Jack meta-ROI). In the longitudinal analysis, Tau^{IQ} provided a substantial increase in power over all SUVR approaches. Tau^{IQ} also demonstrated a more plausible annual change (CN+, 2.0%/y; MCI+, 3.6%/y; dementia+, 2.5%/y) that is consistent with increasing deposition. The clinical trial power calculations demonstrated that Tau^{IQ} would be powered to detect a 25% reduction in tau accumulation with a 2-arm study involving 213 subjects per arm and that a 50% reduction could be detected with 54 subjects per arm. This has significant implications for the use of Tau^{IQ} in clinical trials where tau imaging is being deployed as a pharmacodynamic endpoint to assess the impact of novel therapies. Further, Tau^{IQ} was significantly superior in detecting early tau deposition as evidenced by the increase in effect size for the cross-sectional comparison of the CN− and CN+ groups (+45%) and the longitudinal data from the CN+ (+324%) and MCI− (+205%) groups, which indicate that Tau^{IQ} could play an important role in the stratification of early AD populations for trial entry.

Although Tau_L has been the primary Tau^{IQ} outcome explored in this work, the algorithm also calculates a $LTau_L$ parameter if additional local deposition of tau is present. In this study, 31% of all scans had a nonzero $LTau_L$, and the percentage was higher as disease progressed (CN, 22%; MCI, 35%; dementia, 72%). This parameter will be investigated further in future work but could have value in stratifying subjects into subgroups for clinical trial analysis, and it will be interesting to explore whether these deposits relate more directly to individual clinical deficits of patients.

One limitation of this work is that longitudinal changes in atrophy and their impact on the PET measures were not considered; however, the magnitude of atrophy effects is lower than the changes observed for Tau_L, and these effects are present for both Tau^{IQ} and SUVR. Partial-volume correction methods could theoretically be applied to both SUVR and Tau^{IQ} approaches, and further work

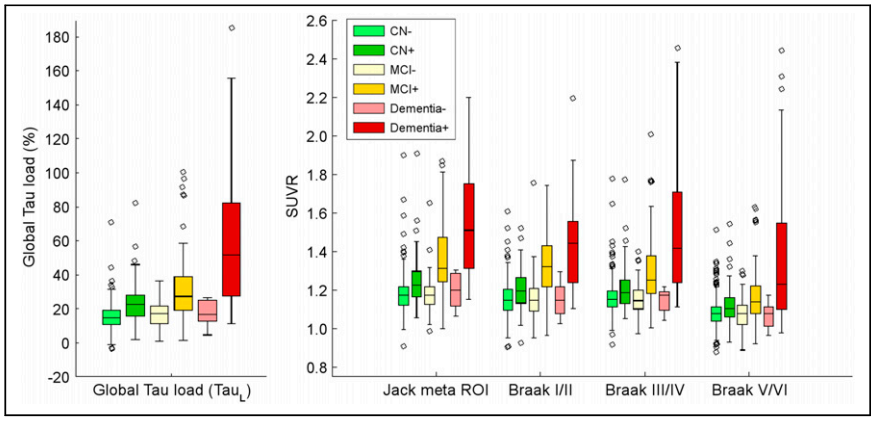

FIGURE 5. Cross-sectional analysis shown as box plots of distributions of ^{18}F-flortaucipir Tau_L and SUVR outcome measures by clinical group.

TABLE 2
Longitudinal Analysis*

Parameter	Tau^{IQ} Tau_L	SUVR Jack meta-ROI	SUVR Braak I/II	SUVR Braak III/IV	SUVR Braak V/VI
CN−					
Mean and SD	**1.20 (2.31)**	0.003 (0.037)	0.001 (0.037)	0.003 (0.036)	−0.001 (0.037)
Effect size and CI	**0.52 (0.28 to 0.79), $P < 0.016$**	0.09 (−0.18 to 0.37)	0.02 (−0.25 to 0.30)	0.08 (−0.19 to 0.37)	−0.02 (−0.30 to 0.24)
n	**940**	33,812	557,745	37,422	847,562
CN+					
Mean and SD	**2.01 (2.97)**	0.009 (0.044)	0.007 (0.039)	0.007 (0.041)	0.007 (0.039)
Effect size and CI	**0.68 (0.43 to 0.98), $P < 0.022$**	0.21 (−0.12 to 0.55)	0.19 (−0.15 to 0.52)	0.18 (−0.16 to 0.55)	0.17 (−0.16 to 0.55)
n	**546**	5,726	6,699	8,170	9,019
MCI−					
Mean and SD	**1.87 (2.28)**	0.008 (0.032)	−0.002 (0.040)	0.004 (0.031)	0.010 (0.025)
Effect size and CI	**0.82 (0.57 to 1.58), $P < 0.13$**	0.24 (−0.22 to 0.82)	−0.04 (−0.49 to 0.53)	0.13 (−0.31 to 0.79)	0.40 (−0.05 to 0.94)
n	**377**	4,458	190,970	14,512	1,610
MCI+					
Mean and SD	**3.61 (3.31)**	0.023 (0.049)	0.008 (0.052)	0.023 (0.047)	0.017 (0.044)
Effect size and CI	**1.09 (0.79 to 1.54), $P < 0.020$**	0.47 (0.12 to 0.85)	0.16 (−0.24 to 0.57)	0.49 (0.13 to 0.93)	0.39 (0.00 to 0.89)
n	**213**	1,130	10,229	1,063	1,655
Dementia−					
Mean and SD	**1.53 (2.43)**	−0.001 (0.032)	−0.007 (0.019)	0.002 (0.024)	0.002 (0.024)
Effect size and CI	**0.63 (−0.13 to 2.14), $P < 0.28$**	−0.04 (−1.55 to 0.76)	−0.34 (−1.32 to 0.76)	0.09 (−1.18 to 1.01)	0.06 (−1.52 to 1.01)
n	**640**	147,860	2,080	29,595	63,426
Dementia+					
Mean and SD	**2.52 (6.64)**	0.004 (0.085)	−0.011 (0.079)	0.002 (0.080)	−0.005 (0.078)
Effect size and CI	**0.38 (−0.17 to 1.42), $P < 0.27$**	0.05 (−0.44 to 0.83)	−0.13 (−0.58 to 0.71)	0.02 (−0.56 to 0.76)	−0.06 (−0.64 to 0.71)
n	**1,741**	99,385	13,985	32,2607	67,106

*Change in ^{18}F-flortaucipir Tau_L and SUVR outcome measures per year for each clinical group. Best-performing method in terms of effect size (mean/SD) is highlighted in bold along with probability that it is the best method. *n* is number of subjects, in both active and placebo arms of simulated clinical trial, required to show 25% reduction in tau accumulation in active arm over period of 1 y (power = 80%, $\alpha = 0.05$).

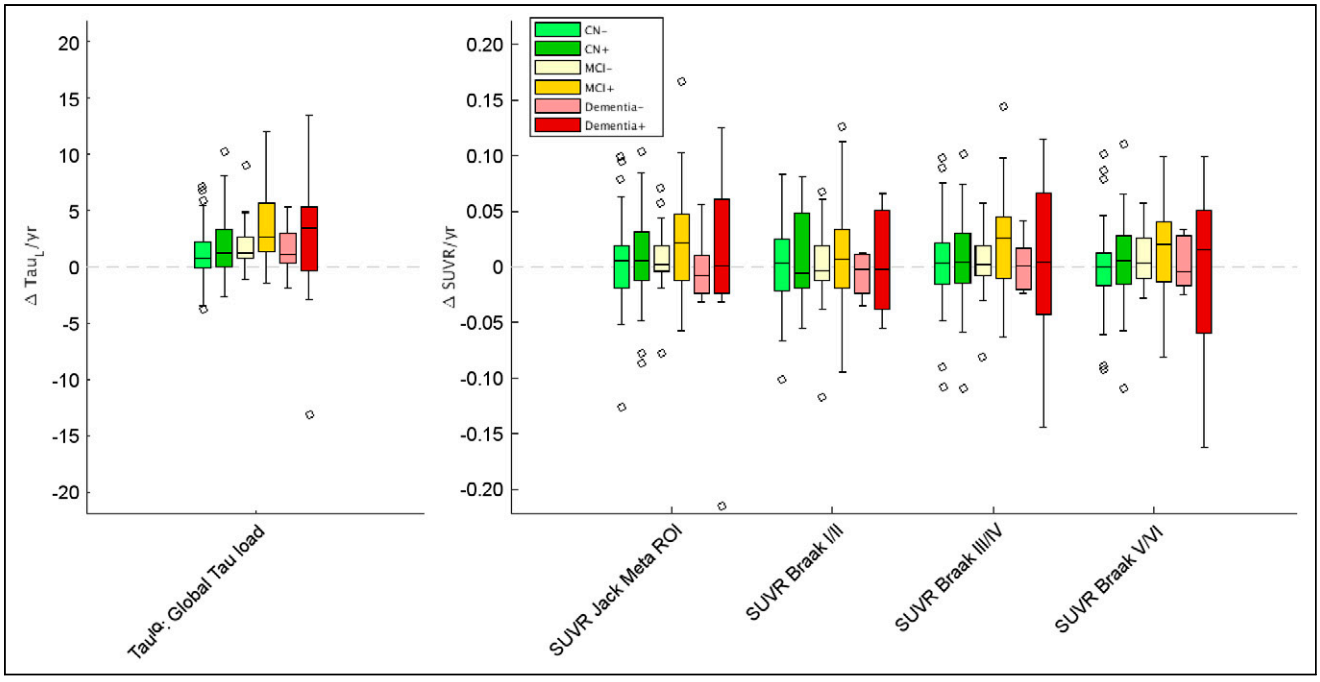

FIGURE 6. Longitudinal analysis shown as box plots of distributions of change in ^{18}F-flortaucipir Tau_L and SUVR outcome measures.

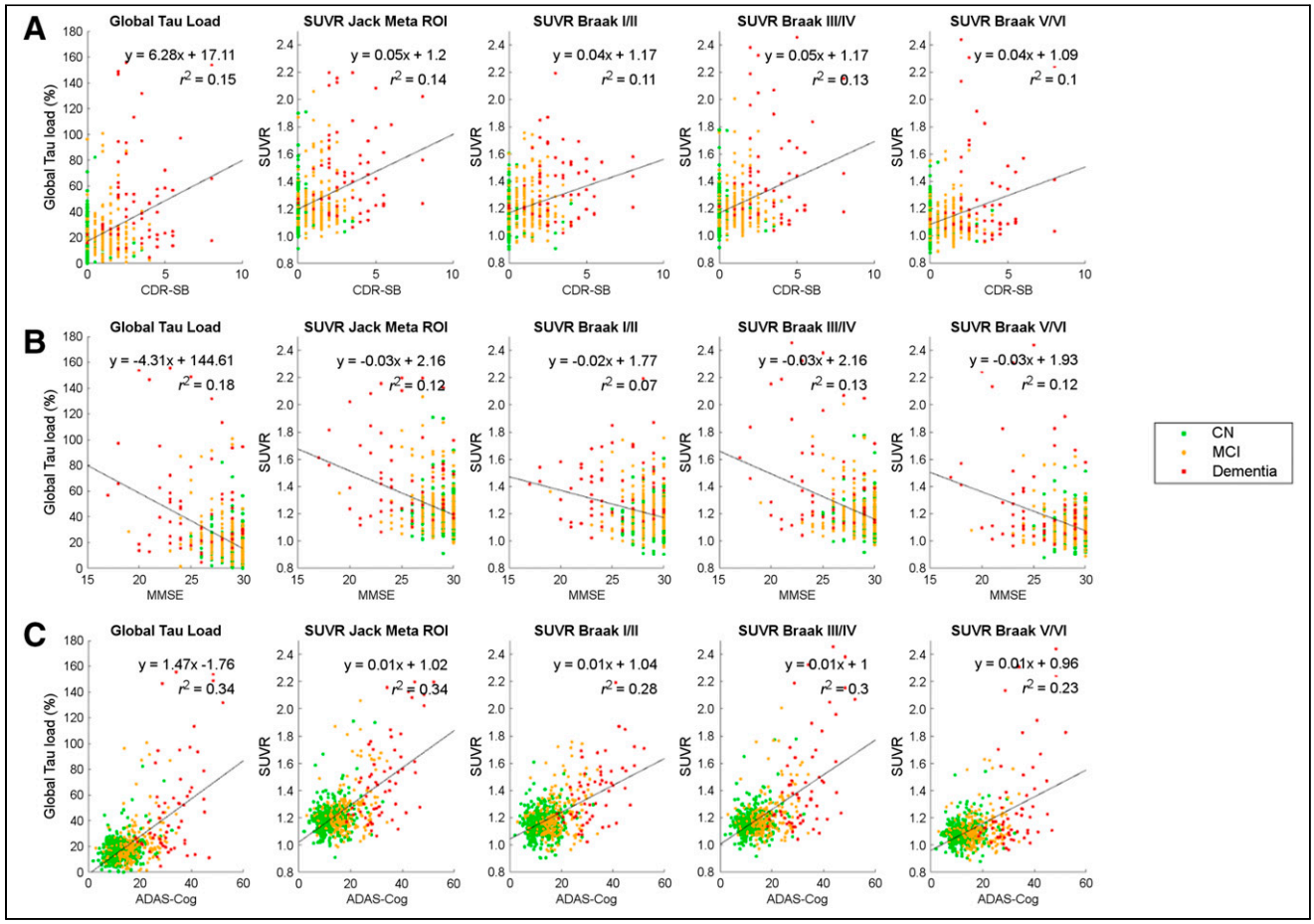

FIGURE 7. Correlations between clinical scores (CDR-SB, MMSE, and ADAS-Cog) and tau imaging outcome measures.

will investigate this possibility. Also, the current analysis used spatially normalized and smoothed images as part of the analytic pipeline. It is possible that further advantages could be obtained through processing of unsmoothed images in native space for both SUVR and Tau^{IQ}.

Although the current work used the tau tracer ^{18}F-flortaucipir, the algorithm is equally applicable to other tau tracers given the appropriate generation of tracer-specific canonical images. Work with the tracer ^{18}F-GTP-1 has also been presented and demonstrated increased performance over SUVR approaches (*34*).

CONCLUSION

Tau^{IQ} is a canonical image-based algorithm for the quantification of tau PET scans and accounts for the more complex deposition of tau than of amyloid. Tau_L as estimated by Tau^{IQ} provides a substantial improvement in power for longitudinal analyses and for early detection of tau deposition over SUVR approaches and should have significant value for clinical imaging trials in AD that are investigating the attenuation of tau deposition with novel therapies.

DISCLOSURE

Data collection and sharing for this project were funded by the ADNI (National Institutes of Health grant U01 AG024904) and DOD ADNI (Department of Defense award W81XWH-12-2-0012). ADNI is funded by the National Institute on Aging, by the National Institute of Biomedical Imaging and Bioengineering, and through generous contributions from the following: AbbVie, Alzheimer's Association; Alzheimer's Drug Discovery Foundation; Araclon Biotech; BioClinica, Inc.; Biogen; Bristol-Myers Squibb Company; CereSpir, Inc.; Cogstate; Eisai Inc.; Elan Pharmaceuticals, Inc.; Eli Lilly and Company; EuroImmun; F. Hoffmann-La Roche Ltd. and its affiliated company Genentech, Inc.; Fujirebio; GE Healthcare; IXICO Ltd.; Janssen Alzheimer Immunotherapy Research & Development, LLC; Johnson & Johnson Pharmaceutical Research & Development LLC; Lumosity; Lundbeck; Merck & Co., Inc.; Meso Scale Diagnostics, LLC; NeuroRx Research; Neurotrack Technologies; Novartis Pharmaceuticals Corporation; Pfizer Inc.; Piramal Imaging; Servier; Takeda Pharmaceutical Company; and Transition Therapeutics. The Canadian Institutes of Health Research provides funds to support ADNI clinical sites in Canada. Private-sector contributions are facilitated by the Foundation for the National Institutes of Health (www.fnih.org). The grantee organization is the Northern California Institute for Research and Education, and the study is coordinated by the Alzheimer's Therapeutic Research Institute at the University of Southern California. ADNI data are disseminated by the Laboratory for Neuro Imaging at the University of Southern California. Alex Whittington is an employee of Invicro. Roger Gunn is an employee of Invicro and a consultant for Abbvie, Biogen, and Cerveau. No other potential conflict of interest relevant to this article was reported.

ACKNOWLEDGMENTS

We thank Jacob Hesterman, John Seibyl, Ken Marek, and Mark Mintun for valuable discussions during this work. Data used in preparation of this article were obtained from the Alzheimer Disease Neuroimaging Initiative (ADNI) database (http://adni.loni.usc.edu). As such, the investigators within the ADNI contributed to the design and implementation of ADNI or provided data but did not participate in analysis or writing of this report. A complete listing of ADNI investigators can be found at https://adni.loni.usc.edu/wp-content/uploads/how_to_apply/ADNI_Acknowledgement_List.pdf.

KEY POINTS

QUESTION: What is the best way of quantifying tau PET images?

PERTINENT FINDINGS: The Tau^{IQ} algorithm introduced in this work shows increased performance over standard SUVR approaches. This quantification approach will provide increased performance when using tau imaging as a biomarker in clinical trials, leading to either studies with fewer subjects or increased signals.

IMPLICATIONS FOR PATIENT CARE: This algorithm might provide data for important clinical decision making when AD therapies become approved.

REFERENCES

1. Klunk WE, Engler H, Nordberg A, et al. Imaging brain amyloid in Alzheimer's disease with Pittsburgh compound-B. *Ann Neurol.* 2004;55:306–319.
2. Klunk WE, Koeppe RA, Price JC, et al. The centiloid project: standardizing quantitative amyloid plaque estimation by PET. *Alzheimers Dement.* 2015;11:1–15.e1.
3. Whittington A, Sharp DJ, Gunn RN. Spatiotemporal distribution of β-amyloid in Alzheimer disease is the result of heterogeneous regional carrying capacities. *J Nucl Med.* 2018;59:822–827.
4. Whittington A, Gunn RN; Alzheimer's Disease Neuroimaging Initiative. Amyloid load: a more sensitive biomarker for amyloid imaging. *J Nucl Med.* 2019;60:536–540.
5. Chien DT, Bahri S, Szardenings AK, et al. Early clinical PET imaging results with the novel PHF-tau radioligand [F-18]-T807. *J Alzheimers Dis.* 2013;34:457–468.
6. Lohith TG, Bennacef I, Vandenberghe R, et al. Brain imaging of Alzheimer dementia patients and elderly controls with ^{18}F-MK-6240, a PET tracer targeting neurofibrillary tangles. *J Nucl Med.* 2019;60:107–114.
7. Sanabria Bohórquez S, Marik J, Ogasawara A, et al. [^{18}F]GTP1 (Genentech Tau Probe 1), a radioligand for detecting neurofibrillary tangle tau pathology in Alzheimer's disease. *Eur J Nucl Med Mol Imaging.* 2019;46:2077–2089.
8. Wong DF, Comley RA, Kuwabara H, et al. Characterization of 3 novel tau radiopharmaceuticals, ^{11}C-RO-963, ^{11}C-RO-643, and ^{18}F-RO-948, in healthy controls and in Alzheimer subjects. *J Nucl Med.* 2018;59:1869–1876.
9. Mueller A, Bullich S, Barret O, et al. Tau PET imaging with ^{18}F-PI-2620 in patients with Alzheimer disease and healthy controls: a first-in-humans study. *J Nucl Med.* 2020;61:911–919.
10. Hsu J-L, Lin K-J, Hsiao I-T, et al. The imaging features and clinical associations of a novel tau PET tracer—^{18}F-APN1607 in Alzheimer disease. *Clin Nucl Med.* 2020;45:747–756.
11. Barthel H. First tau PET tracer approved: toward accurate in vivo diagnosis of Alzheimer disease. *J Nucl Med.* 2020;61:1409–1410.
12. Mattay VS, Fotenos AF, Ganley CJ, Marzella L. Brain tau imaging: Food and Drug Administration approval of ^{18}F-flortaucipir injection. *J Nucl Med.* 2020;61:1411–1412.
13. Braak H, Braak E. Neuropathological stageing of Alzheimer-related changes. *Acta Neuropathol (Berl).* 1991;82:239–259.
14. Jack CR Jr, Wiste HJ, Schwarz CG, et al. Longitudinal tau PET in ageing and Alzheimer's disease. *Brain.* 2018;141:1517–1528.
15. Johnson KA, Schultz A, Betensky RA, et al. Tau positron emission tomographic imaging in aging and early Alzheimer disease. *Ann Neurol.* 2016;79:110–119.
16. Villemagne VL, Fodero-Tavoletti MT, Masters CL, Rowe CC. Tau imaging: early progress and future directions. *Lancet Neurol.* 2015;14:114–124.
17. Schöll M, Lockhart SN, Schonhaut DR, et al. PET imaging of tau deposition in the aging human brain. *Neuron.* 2016;89:971–982.
18. Ossenkoppele R, Schonhaut DR, Schöll M, et al. Tau PET patterns mirror clinical and neuroanatomical variability in Alzheimer's disease. *Brain.* 2016;139:1551–1567.

19. Pontecorvo MJ, Devous MD, Kennedy I, et al. A multicentre longitudinal study of flortaucipir (^{18}F) in normal ageing, mild cognitive impairment and Alzheimer's disease dementia. *Brain.* 2019;142:1723–1735.
20. Sintini I, Martin PR, Graff-Radford J, et al. Longitudinal tau-PET uptake and atrophy in atypical Alzheimer's disease. *Neuroimage Clin.* 2019;23:101823.
21. Harrison TM, La Joie R, Maass A, et al. Longitudinal tau accumulation and atrophy in aging and Alzheimer disease. *Ann Neurol.* 2019;85:229–240.
22. Mueller SG, Weiner MW, Thal LJ, et al. Ways toward an early diagnosis in Alzheimer's disease: the Alzheimer's Disease Neuroimaging Initiative (ADNI). *Alzheimers Dement.* 2005;1:55–66.
23. Jagust WJ, Landau SM, Koeppe RA, et al. The Alzheimer's Disease Neuroimaging Initiative 2 PET Core: 2015. *Alzheimers Dement.* 2015;11:757–771.
24. Mazziotta J, Toga A, Evans A, et al. A probabilistic atlas and reference system for the human brain: International Consortium for Brain Mapping (ICBM). *Philos Trans R Soc Lond B Biol Sci.* 2001;356:1293–1322.
25. Ashburner J. A fast diffeomorphic image registration algorithm. *Neuroimage.* 2007;38:95–113.
26. Tziortzi AC, Searle GE, Tzimopoulou S, et al. Imaging dopamine receptors in humans with [^{11}C]-(+)-PHNO: dissection of D3 signal and anatomy. *Neuroimage.* 2011;54:264–277.
27. Jack CR, Wiste HJ, Lesnick TG, et al. Brain β-amyloid load approaches a plateau. *Neurology.* 2013;80:890–896.
28. Friston KJ, Worsley KJ, Frackowiak RS, Mazziotta JC, Evans AC. Assessing the significance of focal activations using their spatial extent. *Hum Brain Mapp.* 1994;1:210–220.
29. Whittington A, Seibyl J, Gunn RN. Calculation of AβL with the IQAβ algorithm enables automatic and reproducible classification of [^{18}F]-florbetapir scans [abstract]. *Alzheimers Dement.* 2018;14:P503–P504.
30. Lowe VJ, Curran G, Fang P, et al. An autoradiographic evaluation of AV-1451 tau PET in dementia. *Acta Neuropathol Commun.* 2016;4:58.
31. Marquié M, Normandin MD, Vanderburg CR, et al. Validating novel tau positron emission tomography tracer [F-18]-AV-1451 (T807) on postmortem brain tissue. *Ann Neurol.* 2015;78:787–800.
32. Vermeiren C, Motte P, Viot D, et al. The tau positron-emission tomography tracer AV-1451 binds with similar affinities to tau fibrils and monoamine oxidases. *Mov Disord.* 2018;33:273–281.
33. Braak H, Thal DR, Ghebremedhin E, Del Tredici K. Stages of the pathologic process in Alzheimer disease: age categories from 1 to 100 years. *J Neuropathol Exp Neurol.* 2011;70:960–969.
34. Gunn R. TauIQ demonstrates increased power for cross-sectional and longitudinal analysis of tau tracers as evidenced by [18F]flortaucipir and [18F]GTP1. Presented at: Human Amyloid Imaging Conference; January 15, 2020; Miami, FL.